

Stress-strain relationships and yielding of metal-organic framework monoliths

Michele Tricarico¹, Cyril Besnard², Gianfelice Cinque ^{1,3}, Alexander M. Korsunsky ² & Jin-Chong Tan ¹✉

Metal-organic frameworks (MOFs) have emerged as a versatile material platform for a wide range of applications. However, the development of practical devices is constrained by their inherently low mechanical stability. The synthesis of MOFs in a monolithic morphology represents a viable way for the transition of these materials from laboratory research to real-world applications. For the design of MOF-based devices, the mechanical characterization of such materials cannot be overlooked. In this regard, stress-strain relationships represent the most valuable tool for assessing the mechanical response of materials. Here, we use flat punch nanoindentation, micropillar compression and Raman microspectroscopy to investigate the stress-strain behaviour of MOF monoliths. A pseudo-plastic flow is observed under indentation, where the confining pressure prevents unstable crack propagation. Material flow is accommodated by grain boundary sliding, with occasional stepwise cracking to accommodate excessive stress building up. Micropillar compression reveals a brittle failure of ZIF-8, while plastic flow is observed for MIL-68.

¹Multifunctional Materials and Composites (MMC) Laboratory, Department of Engineering Science, University of Oxford, Parks Road, Oxford OX1 3PJ, UK. ²MBLEM, Department of Engineering Science, University of Oxford, Parks Road, Oxford OX1 3PJ, UK. ³Diamond Light Source, Harwell Campus, Chilton, Oxford OX11 0DE, UK. ✉email: jin-chong.tan@eng.ox.ac.uk

Metal-organic frameworks (MOFs) represent a relatively new class of hybrid nanoporous materials, made up of organic ligands and metal clusters that self-assemble into a lattice framework with a significant internal surface area. Several different framework-type compounds with high chemical stability, adjustable physical properties, organic functionality, and porosity have been developed over the past 25 years of research¹, opening up a wide range of potential technological applications^{2–4}, including chemical sensing⁵, gas adsorption⁶, luminescence^{7,8} and energy storage⁹.

Yet, there is not much of a crossover between academic research and industrial practical uses. A poor understanding of the mechanical properties is one of the causes of this shortcoming. The topic of MOF mechanics^{10–12} is still in its infancy despite the extensive research put into the chemical synthesis of new framework structures and the characterization of their functional properties. The primary reason for this relates to the morphological limitations of this class of materials, which are frequently synthesized as polydisperse microcrystalline powders and challenging to characterize using traditional mechanical testing. A way to overcome this limitation is represented by the sol-gel synthesis route, which enables the fabrication of sturdy and bulk monolithic morphologies¹³. Several types of nanoporous sol-gel monoliths have already been reported, including MOFs such as ZIFs (zeolitic imidazolate frameworks)^{14–16}, HKUST-1 (Co-based)¹⁷, UiO-66 (Zr-based)^{18,19} and COFs (covalent organic frameworks)²⁰. This method produces a hierarchical pore distribution, which enhances gas adsorption capabilities²¹.

Most of the mechanical characterization of MOFs to date is based on nanoindentation-based measurements, particularly of Young's modulus (E) and hardness (H), by using the method developed by Oliver and Pharr²². One of the first studies reporting the mechanical properties of a MOF material were carried out by Bahr et al.²³, who characterized MOF-5, a zinc-based framework, and determined a Young's modulus of 7.9 GPa for the (100)-oriented face. Tan et al.²⁴ performed nanoindentation measurements on different types of ZIFs and were able to correlate the mechanical responses with the different ZIF structures (given by the different combinations of organic and inorganic building blocks). Their findings revealed that crystal porosity and linker morphology strongly affect the mechanical properties of the framework. Furthermore, it was demonstrated that the metal sites serve only as compliant nodes for connecting linkages²⁵. Mechanical properties of MOF thin films and coatings have been explored also by nanoindentation^{26,27}.

The literature regarding MOF monoliths mechanics has started to grow in the last few years. Tian et al.¹⁷ performed nanoindentation on a HKUST-1 sol-gel monolith, and measured Young's modulus of $E = 9.3 \pm 0.3$ GPa, which resembles the averaged value predicted from theoretical calculations by density functional theory (DFT) to approximate a randomly oriented polycrystalline bulk material ($E = 8.1$ GPa)²⁸. The monolith hardness ($H = 460$ MPa) is about 130% greater than the HKUST-1 epitaxial film ($H = 200$ MPa) reported by Bundschuh et al.²⁶ Their findings suggest that the high bulk density of the HKUST-1 monolith not only improves the volumetric adsorption capability but also the mechanical resilience. Connolly et al.¹⁸ reported the mechanical properties of UiO-66 monoliths, which were found to vary significantly with drying conditions and washing procedures. In a recent study by some of the authors¹⁵, the mechanical response of two ZIF sol-gel monoliths, namely ZIF-8 and ZIF-71, was analyzed by a combination of nanoindentation, nanoscale Fourier transform infrared spectroscopy (nanoFTIR), tip force microscopy (TFM) and finite element method (FEM) simulations. Grain boundary sliding was found to predominate at low stresses, followed by the collapse/rupture of chemical bonds and a

partial failure of the framework due to shear stresses, which eventually led to the densification of the porous framework at the contact area. In a follow-up study²⁹ the fracture behaviour of MOF monoliths was explored, by analyzing the nanoindentation-induced crack initiation and propagation of four prototypical MOF monoliths (ZIF-8, HKUST-1, MIL-68 and MOF-808), characterized by different framework architectures. A clear correlation between elastic recovery and resistance to crack propagation was observed, with the monoliths exhibiting a low elastic recovery found to be remarkably tough (i.e., MIL-68 and MOF-808). This outstanding ductility was ascribed to a combination of nanostructure (size and shape of nanogranular aggregates) and framework architecture. These factors result in the occurrence of shear faults, most likely in correspondence of the grain boundaries, well contained within the contact area. This localized micro-failure mechanism dissipates energy, hence preventing the initiation of cracks from the indent's corners.

Micropillar compression of MOF glasses³⁰ and single crystals³¹ have been reported recently, but studies of this type are still quite limited due to the susceptibility of MOF-based materials to focused ion beam (FIB) damage.

The aim of this work is to estimate the stress-strain (σ - ϵ) relationships of the two MOF monoliths, namely ZIF-8 and MIL-68, by two different approaches—flat punch indentation and micropillar compression, with the objective of elucidating the yielding and plastic behaviour of this class of materials. The ZIF-8 and MIL-68 monoliths were prepared by a sol-gel process, leveraging the high concentration reaction (HCR) method³², as illustrated schematically in Fig. 1. Optical images of the two monoliths are shown in Supplementary Fig. 1. These two materials are characterized by different fracture behaviour under indentation employing a sharp-tip probe²⁹. Our findings reveal different plastic responses, attributed to the nanogranular structure and the framework architecture. Moreover, confocal Raman microspectroscopy was employed to shed light on the contribution of the framework to the residual strains induced by flat punch indentation.

Results and discussion

Stress-strain relationships by flat punch nanoindentation tests.

The stress-strain behaviour of the two monoliths was estimated by flat-punch (diameter 10.64 μm) nanoindentation tests, following the method developed by Hay (2019)³³, described in detail in Supporting Method 1.

The resulting load-depth (P - h) and stress-strain (σ - ϵ) curves are shown in Fig. 2. The elastic recovery, which is more prominent for ZIF-8, is the key difference when examining the load depth curves (Fig. 2a). For both monoliths, a moderate strain hardening was observed in the σ - ϵ curves (Fig. 2b), particularly for ZIF-8. The results are summarized in Table 1. It should be noted that since these values were calculated using a model conceived for metals (Hollomon's power law: $\sigma = Ke^n$, where K is the strength coefficient and n the strain hardening exponent), they cannot be regarded as absolute material properties. However, these numbers can be used to contrast the plastic (non-reversible) behaviour of the two monoliths: similar yield stresses were recorded for the two materials (88.2 and 90 MPa for ZIF-8 and MIL-68, respectively). Given its higher hardness, ZIF-8 has a relatively higher strength coefficient (K). The ZIF-8 strain hardening exponent (n) is about twice as large as that for MIL-68. This can be attributed to the more flexible structure of the ZIF-8 framework, which makes it more likely to densify (and ultimately collapse)¹⁵, increasing the strength of the monolith. MIL-68, on the other hand, has a stiffer framework and smaller particle size, which leads to an improved ductility²⁹. We suggest

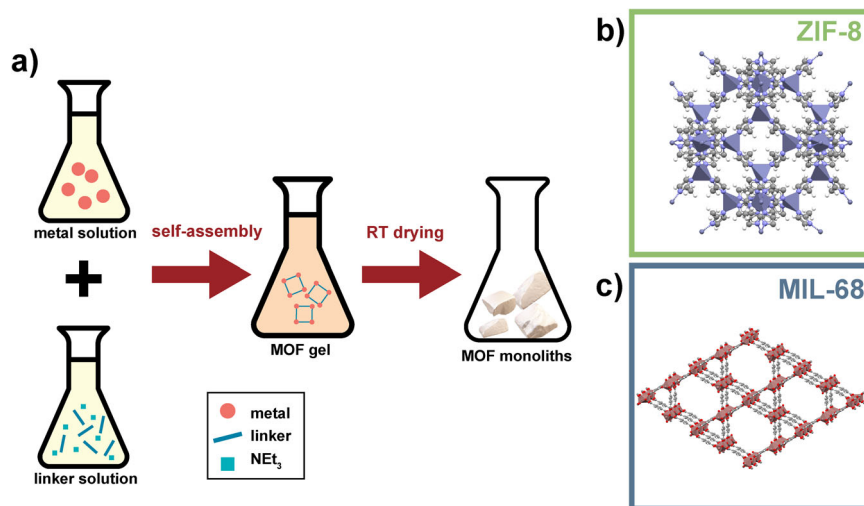


Fig. 1 Schematic of the synthesis of sol-gel MOF monoliths. **a** The high concentration reaction (HCR) synthetic approach involves the deprotonation of the organic linker using a base, i.e. triethylamine (NEt₃), which accelerates the production of metal-organic clusters and subsequently increases the number of nucleation sites, resulting in the formation of nanoparticles small enough to induce the formation of a gel. These nanoparticles coalesce and solidify to form the monolith as the gel dries at room temperature (RT). **b** Cage-type architecture of a unit cell of ZIF-8. **c** Channel-type architecture of the MIL-68 framework.

that the higher flexibility of the ZIF-8 structure compared to MIL-68 may result from the lower coordination number of the zinc metal node compared to the indium counterpart and the lower strength of its coordination bonds. Notably, the flow stress of the monoliths in their fully plastic regime is reasonably constant (plateau in σ - ϵ curves) and corresponds to $\sim 1/3$ of the hardness, in accordance with Tabor theory of elastic-plastic contact³⁴. This finding confirms the results of our previous work¹⁵, where the plastic behaviour of MOF monoliths was well approximated by a simple elastic-perfectly plastic mechanical model.

Another difference between the load-depth curves of the two monoliths can be observed in the very first part of the loading curve (indentation depth <200 nm). Figure 2c illustrates a detailed view of the loading curve in this shallow range and its first derivative, dP/dh : MIL-68 exhibits a stiff response in this range, followed by an evident softening for depths > 200 nm. This is not the case for ZIF-8, which exhibits a softer response, without a drastic change in its slope. We reasoned that this may be due to the higher elastic modulus of the MIL-68 framework, which provides a stiffer response prior to grain boundary sliding taking place.

The residual imprints left by the flat punch on the two monoliths surface are shown in Fig. 2d, e. Concentric ring-shaped cracks are evident in both cases, which resemble the shear faults observed in Vickers residual indents in our previous work²⁹. This suggests that the yielding of these MOF monoliths consists of stepwise microcracking—accommodating excessive build-up of stress—likely taking place at the grain boundaries between the nanocrystals. Such a localized failure mechanism is well contained in the vicinity of the residual imprints and does not lead to critical crack propagation. This is supported by the absence of any pop-ins (i.e., sudden displacement bursts at a constant load) in the load-depth curves, which are typically associated with indentation cracking³⁵. This pseudo-ductility is promoted by the fine granular nanostructure of these materials: the particles size is approximately 100 nm in ZIF-8 and even <100 nm in MIL-68 (Supplementary Figs. 2, 3).

Raman microspectroscopy analysis of residual strains. The two materials, characterized by different framework architectures (Fig. 1b, c), exhibited a different vibrational spectral behaviour:

we noticed shifts of some of characteristic Raman bands in ZIF-8 when the Raman probe was moving from outside to inside of the indent (Fig. 3), while the position of all the MIL-68 bands (Fig. 4) was not affected.

Let us analyze in detail the ZIF-8 Raman spectrum. As reported by Chen et al.³⁶ in an in situ study of the effect of high pressure on ZIF-8 crystalline powders, the majority of the bands are due to methyl group ($-\text{CH}_3$) and imidazolite (Im) ring vibrations. The low-frequency bands (176, 284 and 422 cm^{-1}) are ascribed to the vibrations of the ZnN₄ tetrahedra. A detailed assignment of the bands is provided in Table 2.

Our results (Fig. 3) can be compared with the ones reported by Chen et al.³⁶, which observed the evolution of Raman bands with in situ high pressure via a diamond anvil cell, up to ~ 20 GPa. In our case, the maximum pressure applied by the punch is appreciably smaller (of the order of only 0.1–0.2 GPa) and the material underwent an elastic recovery before the measurement. Despite these differences in the pressure range, some similarities can still be observed. First, a broadening of all the vibrational bands was observed inside the indent due to compression, as expected. As shown in Fig. 3 and Supplementary Figs. 5, 6, blue shifts, caused by bond compression, were observed for the Zn-N vibrations (176 cm^{-1}), Im ring puckering (686 cm^{-1}) and out-of-plane bending (1024 cm^{-1}). Interestingly, red shifts—usually related to a state of tension of the bonds³⁷—were observed for two of the bands relative to the C-H out-of-plane bending vibrations in the Im ring (836 cm^{-1} and 953 cm^{-1}), C-N stretching vibration in the Im ring (1146 cm^{-1} and 1185 cm^{-1}), C-H wagging in the methyl group (1461 cm^{-1}), C=C stretching in the Im ring (1500 cm^{-1}) and C-H stretching in the Im ring (3114 cm^{-1} and 3135 cm^{-1}). The red shifts mostly correspond to the stretching vibrations in the linker (Im ring): this is due to the particular mechanical instability of the ZIF-8 framework, which is characterized by an extremely low shear modulus²⁵ and it undergoes shear-mode softening under compression³⁸. We reasoned that the shear-induced deformation of the framework induces a state of tension in the organic linkers.

It is worth noting that the indentation does not induce any residual strain of the crystal structure outside the contact area. This finding suggests that the plastic flow consists of shear-driven

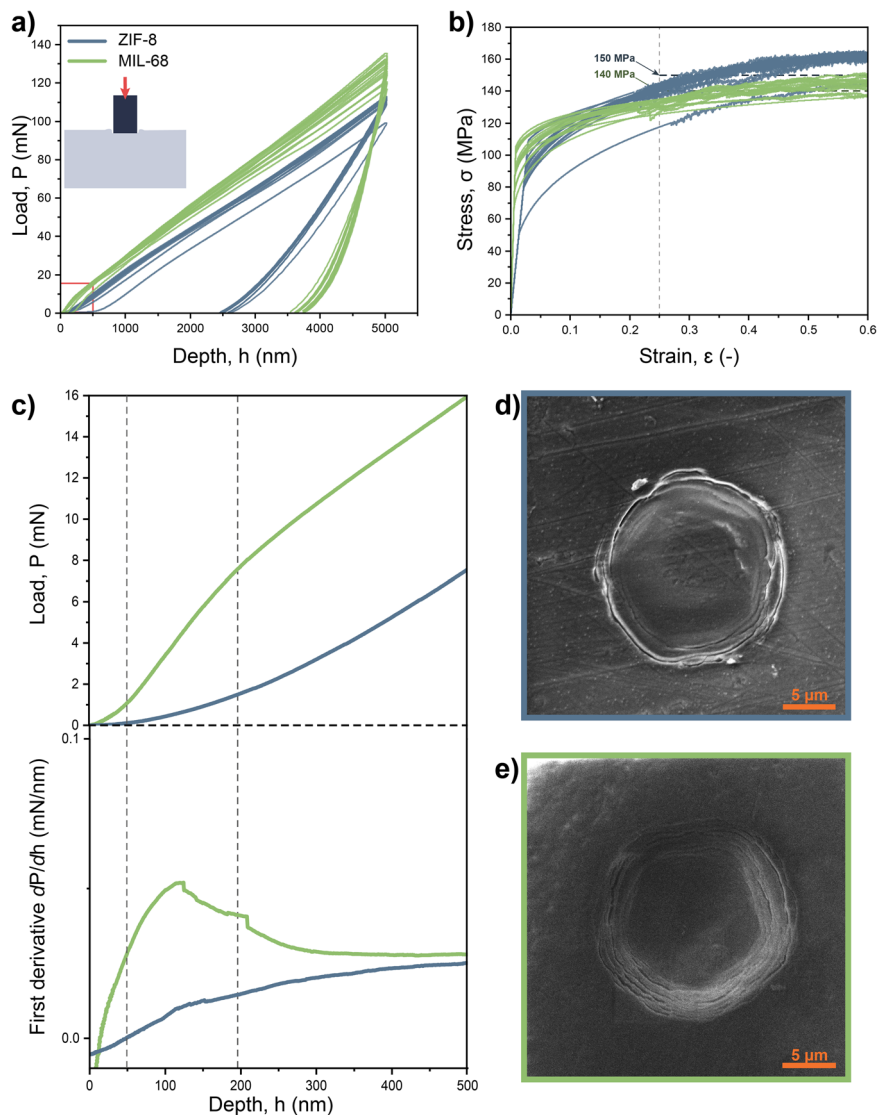


Fig. 2 Flat punch nanoindentation tests on MOF monoliths. **a** Load-depth and **(b)** stress-strain curves resulting from nanoindentation tests of ZIF-8 and MIL-68 monoliths using a flat punch indenter (diameter 10.64 μm). **c** Magnification of two representative load-depth ($P-h$) curves in the range of 0–500 nm (top) and their first derivative, dP/dh (bottom). **d, e** SEM images of some representative residual flat punch imprints on ZIF-8 and MIL-68, respectively.

Table 1 Mechanical properties of ZIF-8 and MIL-68 monoliths extrapolated from the stress-strain curves obtained by flat punch nanoindentation.

Material	Number of tests	Yield stress (MPa)	Yield strain (-)	K (MPa)	n (-)	Average flow stress (MPa)	Hardness (MPa)
ZIF-8	18	88.2 ± 16.4	0.0238 ± 0.0033	184.1 ± 9.5	0.1976 ± 0.0405	140 ± 10	452 ± 20^{15}
MIL-68	16	90.0 ± 10.5	0.0072 ± 0.0008	154.0 ± 6.6	0.1093 ± 0.029	150 ± 16	402 ± 13^{29}

The values of hardness were computed by Berkovich nanoindentation in previous studies^{15,29}.

grain boundary sliding, and rearrangement of the nanograins to accommodate the applied shear strain¹⁵.

On the other hand, the Raman spectra of MIL-68 (Fig. 4) determined from the inside and outside the indent are identical, except for some amount of peak broadening (Supplementary Figs. 7, 8). To the best of our knowledge, no Raman studies of the structural stability of MIL-68 are available so far. Hu et al.³⁹ analyzed the behaviour of MIL-68 under high pressure in a

diamond anvil cell by FTIR spectroscopy. They observed a full recovery of the structure upon releasing the pressure for the as-made sample (i.e., prior to activation, with some DMF still trapped in the channels), while the spectrum of activated MIL-68 was irreversibly modified, especially the O–H stretching mode, which is more sensitive to compression. The peaks relative to O–H stretching were strongly broadened and their intensity decreased already with a small pressure of 0.12 GPa (comparable to the value

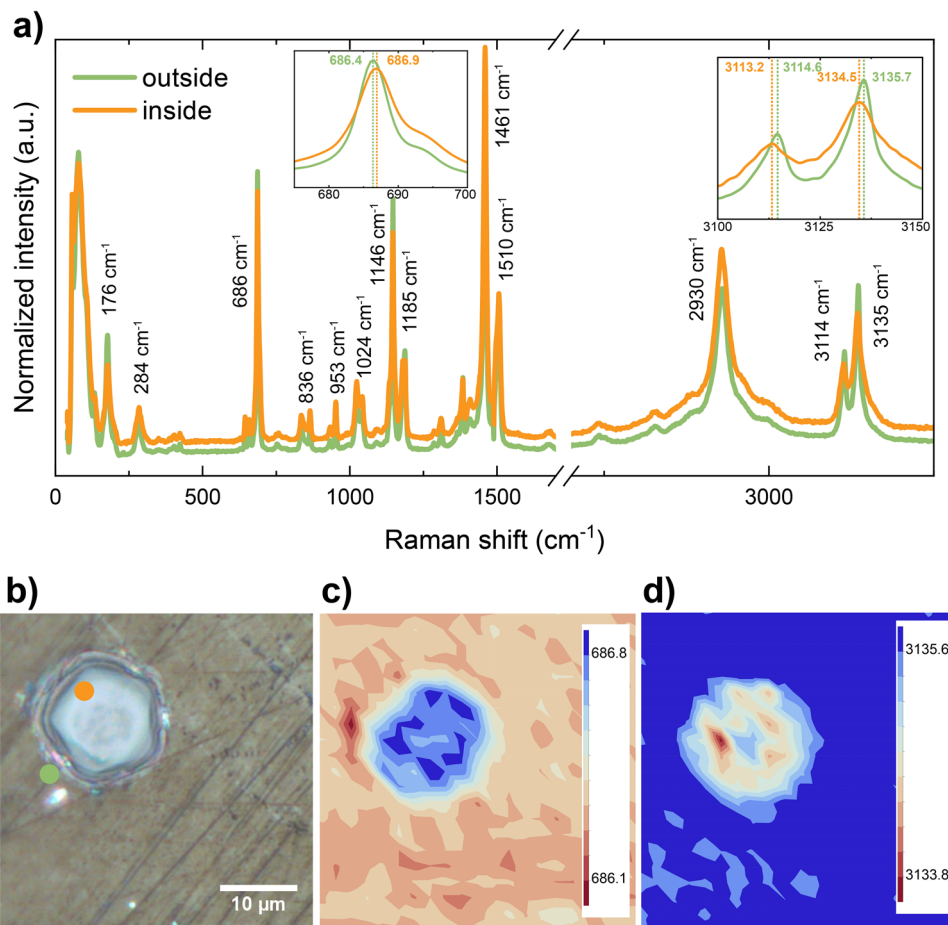


Fig. 3 Confocal Raman microscopy of a flat punch residual imprint on ZIF-8 monolith. **a** Representative Raman spectra taken outside and inside the residual indent. The insets show details of the stress-induced blue-shift of the 686 cm^{-1} band (1m ring puckering) and red-shift of the 3114 cm^{-1} and 3135 cm^{-1} bands (C–H stretching in the 1m ring). **b** Optical micrograph of the indent. **c, d** Contour maps indicating the spectral shift of some of the characteristic phonon bands of ZIF-8, i.e., 686 cm^{-1} and 3135 cm^{-1} , respectively.

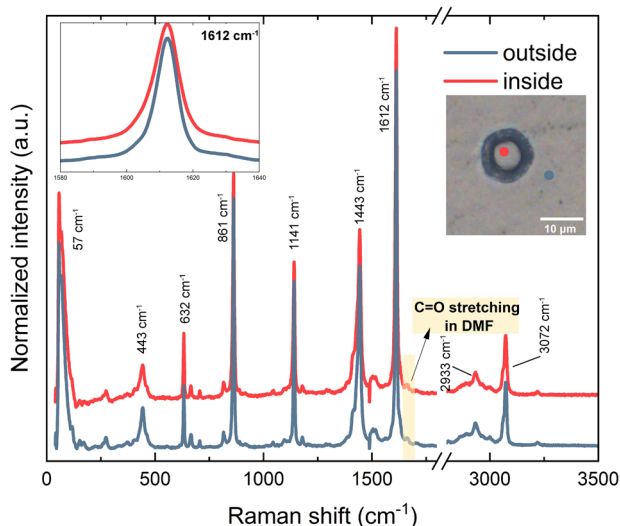


Fig. 4 Confocal Raman microscopy of a flat punch residual imprint on MIL-68 monolith. Representative Raman spectra of a MIL-68 monolith taken outside and inside a residual flat punch imprint. The inset shows a magnified view of the 1612 cm^{-1} band, revealing the absence of stress-induced shifts.

applied by our nanoindentation test). This suggests a significant guest-host interaction in the porous framework upon compression. The absence of major changes in the Raman spectrum in our case suggests a complete recovery of the framework structure, facilitated by the presence of some residual DMF molecules retained in the channels, demonstrated by the (weak) band at $\sim 1661\text{ cm}^{-1}$ (C = O stretching in DMF^{40,41}), as highlighted in Fig. 4.

As a control experiment, the effect of pressure on ZIF-8 and MIL-68 monoliths was studied by means of bulk ATR-FTIR (Supplementary Fig. 9 and Supplementary Fig. 12), XRD (Supplementary Fig. 10 and Supplementary Fig. 13) and Raman spectroscopy (Supplementary Fig. 11, Supplementary Fig. 14 and Supplementary Table 3) and discussed in the Supporting Note 1. The significance of DMF becomes particularly obvious in the IR spectra: the intensity of the band relative to the C = O stretching in DMF ($\sim 1673\text{ cm}^{-1}$) is not significantly reduced with increasing pressure in MIL-68 (Supplementary Fig. 12), unlike ZIF-8 (Supplementary Fig. 9). This might imply that solvent is still trapped inside the channels of the MIL-68 framework. Also in this case, shifts of the framework characteristic Raman bands were observed in ZIF-8 but not in the case of MIL-68.

Micropillar compression. Two sets of micropillars were fabricated on each sample, see Supplementary Fig. 15. Scanning

Table 2 Raman bands correlation table for ZIF-8.

Approximate wavenumber (cm ⁻¹)	Mode assignments
176	Vibrations of the ZnN ₄ tetrahedra
284	
422	
686	
694	Im ring puckering
836	
953	C–H out-of-plane bending vibration in the Im ring
1024	
1146	C–N stretching vibration in the Im ring
1185	
1461	C–H wagging in the methyl group
1500	C=C stretching in the Im ring
2930	C–H stretching in the methyl group
3114	C–H stretching in the Im ring
3135	(aromatic group)

electron microscopy (SEM) micrographs of the micropillars before and after the test were taken for both ZIF-8 (Supplementary Figs. 16–19) and MIL-68 (Supplementary Figs. 20–23). The load–displacement curves resulting from each test are shown in Supplementary Figs. 26 and 27 for ZIF-8 and MIL-68, respectively. These curves were converted into the nominal (σ – ϵ) curves (Fig. 5a–c), using the following relationships:

$$\sigma = \frac{P}{(\pi d^2/4)} \quad (1)$$

$$\epsilon = \frac{h}{l} \quad (2)$$

where P is the load, d the pillar diameter, h the vertical displacement and l the pillar height. The resulting σ – ϵ curves (Fig. 5a and b for ZIF-8 and MIL-68, respectively) showed good reproducibility, particularly the elastic behaviour.

The averaged values of the material properties (namely Young's modulus, yield stress, stress and strain at failure) extracted from micropillar compression tests are listed in Table 3. Values measured for each pillar, along with test inputs are summarized in Supplementary Table 2.

ZIF-8 exhibited a brittle behaviour (Fig. 5a): pop-in events caused by the propagation of cracks, that are visible during elastic loading, are followed by a second, less steep, linear (elastic) segment, indicating that the material response is still elastic but that a smaller cross-sectional area is now bearing the applied load. As we can observe in Fig. 5d and Supplementary Fig. 24, the cracks propagate along the longitudinal direction of the pillars, essentially splitting it in two, hence reducing the cross-sectional area bearing the load. The pillars that were brought to failure (see Supplementary Table 2) were all ruptured at ~17% strain. This different response compared to nanoindentation (brittle rather than pseudo-ductile) is due to the different stress states generated by the two tests: uniaxial for micropillar compression and triaxial for nanoindentation. The latter results in a confining pressure that compacts the nanocrystals, improving the overall toughness.

The strain rate was found to influence the yield stress of ZIF-8 (in this case, defined as the stress at which the first pop-in appears), which decreased by ~30% (from ~200 to ~135 MPa) when the strain rate was reduced from 0.2 to 0.001 s⁻¹. The effect of strain rate might be explained with an inertial effect, similar to what is widely observed in rock-like materials (i.e., solid aggregates of minerals)⁴². Inertia initially inhibits crack growth, meaning that the cracks will have less time to nucleate at higher strain rate, hence starting to propagate at higher stresses.

The stress–strain behaviour of MIL-68 was very different from ZIF-8. As shown in Fig. 5b, there is a significant plastic deformation (large strains lying within the 20–50% range) and no pop-ins are observed. There is no evidence of longitudinal cracks (Fig. 5e and Supplementary Fig. 25), as opposed to ZIF-8. Two pillars failed (set #1—pillar #1 and set #2—pillar #1) and their fracture surfaces (Supplementary Figs. 20, 21 and Supplementary Figs. 22, 23, respectively) suggest that the pillars cracked in the direction perpendicular to their axis, contrary to what was observed for ZIF-8 (Supplementary Fig. 24c, d), with the pillar failing after longitudinal splitting. Particularly noteworthy is the case of pillar #1 of set #2 (Supplementary Fig. 25c), that was not crushed like the others, but rather cut at its base. This outcome may suggest a buckling failure, given the greater slenderness of this pillar ($h/l = 2.6$, against ~1 of the others).

These results are in good agreement with what was reported in the authors' previous work²⁹, concerning the indentation fracture toughness of these two monoliths. ZIF-8 was found to be more susceptible to sharp indentation cracking than MIL-68. The different fracture behaviour was ascribed to the different framework architectures and nanostructures, resulting in distinct elastic-plastic behaviours: ZIF-8 is characterized by large elastic recovery and high H/E ratio, distinctive features of brittle materials, contrary to MIL-68 (low elastic recovery and low H/E), which exhibits an extraordinary resistance to indentation cracking. The ductility of MIL-68 stems from the small size and morphology of the nanoparticles building blocks and the stiff and robust nature of the framework: this combination promotes the grain boundary sliding as principal deformation mechanism. This dramatically reduces the share of load transferred to the framework, avoiding its distortion and eventual collapse, as confirmed by the microRaman results, where no stress-induced spectral modifications were observed.

The Young's modulus values measured by the σ – ϵ curves obtained from micropillar compression (measured as the slope of the linear segments, before pop-ins) are lower than the results for ZIF-8 and MIL-68 monoliths based on traditional nanoindentation^{15,29}, particularly for MIL-68, for which it is only 20% of the counterpart measured by nanoindentation. Young's modulus of ZIF-8 was $E = 2.45 \pm 0.34$ GPa, (against 3.18 ± 0.04 GPa¹⁵ measured by nanoindentation) and the one of MIL-68 was 2.28 ± 0.37 GPa, (against 13.24 ± 0.52 GPa²⁹ measured by nanoindentation). Numerous studies have found that the modulus values for micropillars compression are significantly lower than those for nanoindentation^{43–46}, due to the intrinsic differences between the two methods. Moreover, in the case of self-assembled nanoparticles-based materials, like the monoliths analyzed in this work, FIB milling induces the formation of highly porous network, caused by the nanoparticles migration and melting upon ion beam exposure⁴⁷. This phenomenon was observed in both ZIF-8 and MIL-68 samples, as porous networks are visible inside the trenches surrounding the pillars (Fig. 5d, e and Supplementary Figs. 24, 25). The presence of these features may affect the computation of strain since the actual height of the pillars may be higher than the measured one. Finally, there may be some experimental aspects that are material specific. The vacuum pumping in SEM might damage the porous monoliths containing entrapped solvent. This could lead to further loss of stiffness.

Conclusions

The stress–strain relationships of two prototypical MOF monoliths, namely ZIF-8 and MIL-68, obtained by a sol-gel synthesis route, were evaluated by flat-punch indentation and micropillar compression. Under indentation, when a confining pressure is

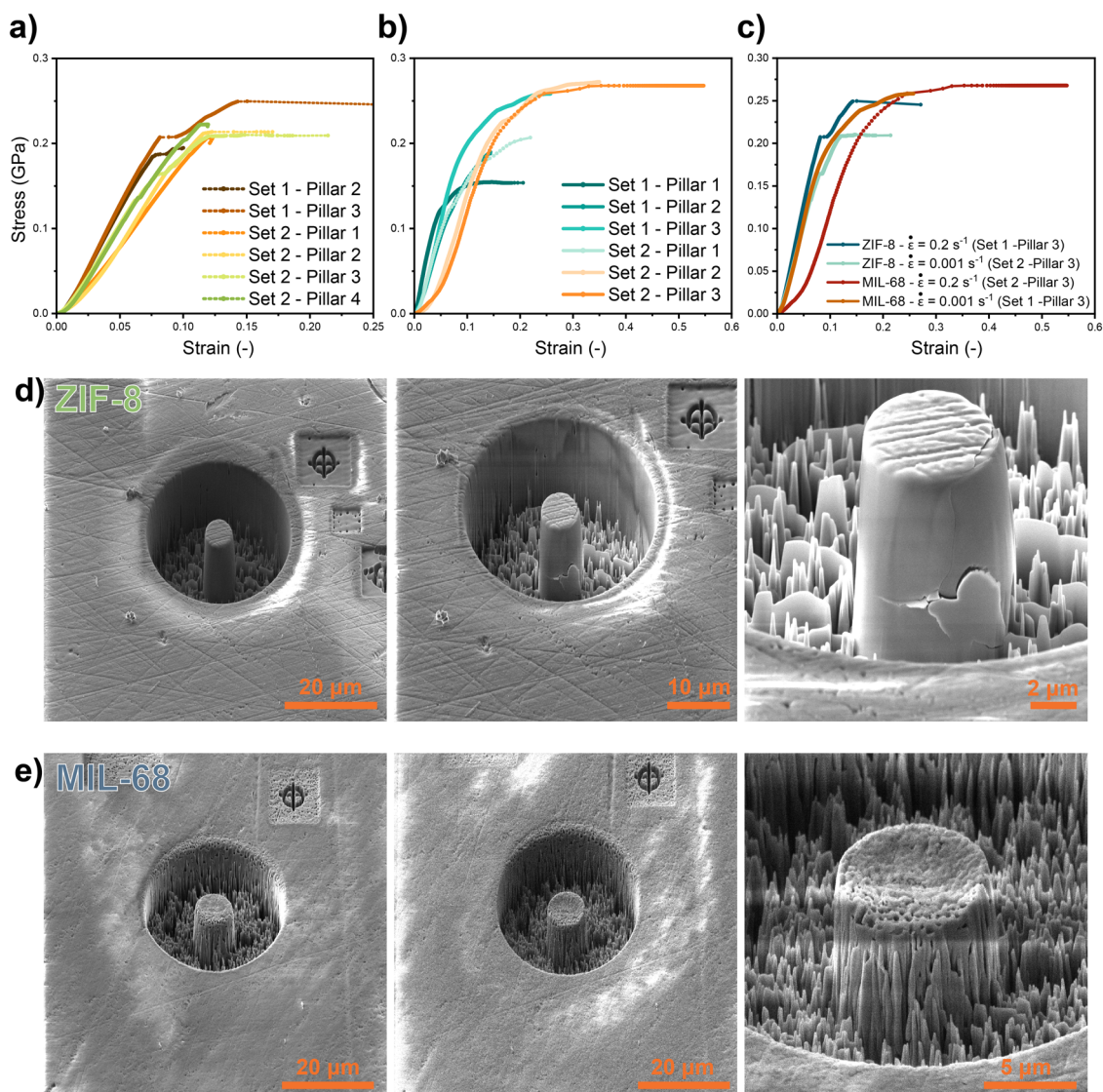


Fig. 5 Micropillar compression tests. **a, b** Stress-strain curves of the micropillars compression of ZIF-8 and MIL-68, respectively. **c** Comparison of some representative ZIF-8 and MIL-68 stress-strain curves, obtained by compression under different strain rates. **d, e** Representative pillars before microcompression test (left), after test (middle) and magnified views of the ZIF-8 and MIL-68 monoliths after the tests (right).

Table 3 Mechanical properties of ZIF-8 and MIL-68 monoliths extrapolated from the micropillar compression tests.

Material	Young's modulus (GPa)	Yield stress (MPa)	Stress at failure (MPa)	Strain at failure (-)
ZIF-8	2.45 ± 0.34	173 ± 30	224 ± 18	0.169 ± 0.015
MIL-68	2.28 ± 0.37	154 ± 38	180 ± 27	0.215 ± 0.007

present and crack propagation is constrained, both the materials display a similar plastic behaviour, characterized by a minimal amount of strain hardening. Consistent with previous studies, this kind of behaviour is promoted by the nanostructure of the sol-gel monoliths, which favours grain boundary sliding as the main deformation mechanism. When the framework itself is compliant enough, it can permanently deform, absorbing part of the applied load. This phenomenon was observed in the ZIF-8 monolith, as demonstrated by the microRaman analysis of the residual flat punch indent, which evidenced the presence of residual strains at the framework level. Micropillar compression resulted in two different yielding behaviours: ZIF-8 fails by elastic crack

propagation, while MIL-68 exhibits a certain amount of plastic flow prior to failure.

The results of this work will broaden the current understanding of the mechanical behaviour of MOF monoliths and nanocrystalline porous materials in general, which is a nascent field, but will underpin the core development of this class of materials from academic research to real-world applications.

Methods

Materials synthesis. Zinc nitrate hexahydrate ($\text{Zn}(\text{NO}_3)_2 \cdot 6\text{H}_2\text{O}$), 2-methylimidazole (mIm), indium nitrate, 1,4-benzenedicarboxylate

(BDC), triethylamine (NEt₃), dimethylformamide (DMF), methanol (MeOH), and acetonitrile (MeCN) were purchased from Fisher Scientific and used as received.

ZIF-8 monoliths were synthesized following the procedure described in our previous work¹⁵: 0.595 g of Zn(NO₃)₂·6H₂O and 0.493 g of mIm were dissolved in 9 mL of DMF each and stirred for 5 min. Then, 0.837 mL of triethylamine (NEt₃) were added to the linker solution. Subsequently, the two solutions were combined in a 50 mL vial, where a gel was promptly formed. The mixture was sonicated for 5 min and then washed three times, in 50 mL of solvent (DMF, MeOH and MeCN, respectively), followed by centrifugation at 8000 rpm. The collected solid was dried slowly at room temperature (RT ~ 25 °C) for 3 days under the fume cupboard to yield monoliths.

MIL-68(In) monoliths following the procedure reported in our previous work²⁹: a 9 mL DMF solution of 797 mg of 1,4-benzenedicarboxylic acid (H₂BDC) plus NEt₃ (9.6 mmol) was prepared. After that, 9 mL DMF solution of 1444 mg of indium nitrate was immediately added into the mixture. Then the product was washed thoroughly 4 times (2 times with DMF, 2 times with MeOH). The nanocrystals of MIL-68(In) were separated from the suspension by centrifugation at 8000 rpm for 10 min and the excess solvent was decanted. The obtained material was dried at room temperature for 3 days to yield monoliths.

Nanoindentation. Nanoindentation tests were carried out using an iMicro nanoindenter (KLA-Tencor) equipped with a 1 N load cell. The as-synthesized monoliths were cold mounted in epoxy resin (Struers Epofix), resulting in cylindrical samples. The specimens were thoroughly polished with sandpapers and diamond suspensions (up to a 0.1 μm surface finish) to minimize roughness and obtain a flat surface suitable for nanoindentation.

A flat punch indenter was employed, (diameter 10.64 μm) in accordance with the method patented by Hay (2019)³³ to estimate stress-strain relationships. The flat punch indenter was pressed into the surface at a constant strain rate of 0.005 s⁻¹ to a maximum depth of 5000 nm. More details of the method are given in the Supporting Method 1.

Pellet preparation. ZIF-8 and MIL-68 pellets were produced by using a manual hydraulic press (Specac). 100 mg of powder materials (obtained by gently grinding the monoliths) per pellet were compressed under pressures of 0.075, 0.15 and 0.375 GPa.

Confocal Raman microscopy (microRaman). Raman microspectroscopy measurements were performed at beamline B22, Diamond Light Source (DLS), Didcot (UK), using a confocal Bruker Senterra Raman microscope. The mapping of the residual flat punch indents was collected by setting the following measurements conditions: objective 50×, laser 532 nm with grating 1200, resolution 3–5 cm⁻¹, laser power 12 mW, integration time 5000 ms, scan area 40 μm × 40 μm, 21 × 21 points, and confocal aperture of 25 × 25 μm.

Averaged Raman spectra of the pellets were obtained by collecting 20 spectra per sample, in different areas. In this case a ×20 objective was employed and a 5 s bleaching step was necessary for baseline corrections. All the other parameters were kept constant.

XRD. X-ray diffraction (XRD) patterns were recorded using a Rigaku MiniFlex with a Cu Kα source (1.541 Å).

ATR-FTIR. Attenuated total reflection Fourier Transform Infrared (ATR-FTIR) spectra were recorded using a Nicolet iS10 FTIR spectrometer (employing a diamond crystal).

SEM and FIB. Scanning electron microscopy (SEM) images of the nanocrystalline aggregates were acquired with a Tescan Lyra 3 (Tescan, Czech Republic) field-emission scanning electron microscope, operating under a voltage of 10 keV. Focused Ion Beam (FIB) was used to fabricate the micropillars for compression testing. The voltage was set to 30 keV, the values of beam current are listed in Supplementary Table 1.

Micropillar compression. Compression tests of the micropillars were performed by a flat punch indenter (diameter 10.64 μm), using an iMicro nanoindenter (KLA-Tencor), equipped with a 50 mN load cell.

AFM imaging. The surface topography of the monoliths and the nanocrystal aggregates was studied by atomic force microscopy (AFM) as implemented in a neaSNOM instrument (neaspec GmbH), in tapping-mode. A Scout350 (NuNano) probe with a nominal tip radius of 5 nm and a resonance frequency of 350 kHz was used.

The surface of the monoliths was imaged using the same samples used for nanoindentation. The nanocrystal aggregates samples were prepared by drop-casting: a small quantity of gel (~1 mL) was pipetted out of the vial before drying and diluted with a large volume of solvent (~20 mL), yielding a dispersion of nanocrystals. The dispersion was then drop casted on a silicon wafer (~1 cm × 1 cm), which had been carefully cleansed to eliminate dust and other surface impurities beforehand. Following that, the silicon chip was air dried in a fume hood.

Data availability

The primary data that support the findings of this study are available within the Supplementary Information and from the corresponding author upon reasonable request.

Received: 12 June 2023; Accepted: 3 October 2023;

Published online: 18 October 2023

References

1. Freund, R. et al. 25 years of reticular chemistry. *Angew. Chem. Int. Ed.* **60**, 23946–23974 (2021).
2. Falcaro, P. et al. MOF positioning technology and device fabrication. *Chem. Soc. Rev.* **43**, 5513–5560 (2014).
3. Stassen, I. et al. An updated roadmap for the integration of metal-organic frameworks with electronic devices and chemical sensors. *Chem. Soc. Rev.* **46**, 3185–3241 (2017).
4. Bavykina, A. et al. Metal-organic frameworks in heterogeneous catalysis: recent progress, new trends, and future perspectives. *Chem. Rev.* **120**, 8468–8535 (2020).
5. Olorunoyi, J. F., Geh, S. T., Caruso, R. A. & Doherty, C. M. Metal-organic frameworks for chemical sensing devices. *Mater. Horiz.* **8**, 2387–2419 (2021).
6. Petit, C. Present and future of MOF research in the field of adsorption and molecular separation. *Curr. Opin. Chem. Eng.* **20**, 132–142 (2018).
7. Yan, B. Photofunctional MOF-based hybrid materials for the chemical sensing of biomarkers. *J. Mater. Chem. B* **7**, 8155–8175 (2019).
8. Gutierrez, M., Zhang, Y. & Tan, J. C. Confinement of luminescent guests in metal-organic frameworks: understanding pathways from synthesis and multimodal characterization to potential applications of LG@MOF systems. *Chem. Rev.* **122**, 10438–10483 (2022).
9. Zhang, X. et al. Metal-organic frameworks (MOFs) and MOF-derived materials for energy storage and conversion. *Electrochem. Energ. Rev.* **2**, 29–104 (2019).
10. Tan, J.-C. in *Mechanical Behaviour of Metal-Organic Framework Materials* (ed Tan, J.-C.) 1–64 (The Royal Society of Chemistry, 2023).
11. Burtch, N. C., Heinen, J., Bennett, T. D., Dubbeldam, D. & Allendorf, M. D. Mechanical properties in metal-organic frameworks: emerging opportunities and challenges for device functionality and technological applications. *Adv. Mater.* **30**, 1704124 (2018).

12. Redfern, L. R. & Farha, O. K. Mechanical properties of metal–organic frameworks. *Chem. Sci.* **10**, 10666–10679 (2019).
13. Hou, J., Sapnik, A. F. & Bennett, T. D. Metal–organic framework gels and monoliths. *Chem. Sci.* **11**, 310–323 (2020).
14. Tian, T., Velazquez-Garcia, J., Bennett, T. D. & Fairen-Jimenez, D. Mechanically and chemically robust ZIF-8 monoliths with high volumetric adsorption capacity. *J. Mater. Chem. A* **3**, 2999–3005 (2015).
15. Tricarico, M. & Tan, J.-C. Mechanical properties and nanostructure of monolithic zeolitic imidazolate frameworks: a nanoindentation, nanospectroscopy, and finite element study. *Mater. Today Nano* **17**, 100166 (2022).
16. Mehta, J. P. et al. Sol-gel synthesis of robust metal-organic frameworks for nanoparticle encapsulation. *Adv. Funct. Mater.* **28**, 1705588 (2018).
17. Tian, T. et al. A sol-gel monolithic metal-organic framework with enhanced methane uptake. *Nat. Mater.* **17**, 174–179 (2018).
18. Connolly, B. M. et al. Tuning porosity in macroscopic monolithic metal-organic frameworks for exceptional natural gas storage. *Nat. Commun.* **10**, 2345 (2019).
19. Bueken, B. et al. Gel-based morphological design of zirconium metal-organic frameworks. *Chem. Sci.* **8**, 3939–3948 (2017).
20. Carrington, M. E. et al. Sol-gel processing of a covalent organic framework for the generation of hierarchically porous monolithic adsorbents. *Chem.* **8**, 2961–2977 (2022).
21. Connolly, B. M., Madden, D. G., Wheatley, A. E. H. & Fairen-Jimenez, D. Shaping the future of fuel: monolithic metal-organic frameworks for high-density gas storage. *J. Am. Chem. Soc.* **142**, 8541–8549 (2020).
22. Oliver, W. C. & Pharr, G. M. An improved technique for determining hardness and elastic modulus using load and displacement sensing indentation experiments. *J. Mater. Res.* **7**, 1564–1583 (1992).
23. Bahr, D. F. et al. Mechanical properties of cubic zinc carboxylate IRMOF-1 metal-organic framework crystals. *Phys. Rev. B* **76**, 184106 (2007).
24. Tan, J. C., Bennett, T. D. & Cheetham, A. K. Chemical structure, network topology, and porosity effects on the mechanical properties of Zeolitic Imidazolate Frameworks. *Proc. Natl. Acad. Sci. USA* **107**, 9938–9943 (2010).
25. Tan, J. C. et al. Exceptionally low shear modulus in a prototypical imidazole-based metal-organic framework. *Phys. Rev. Lett.* **108**, 095502 (2012).
26. Bundschuh, S. et al. Mechanical properties of metal-organic frameworks: an indentation study on epitaxial thin films. *Appl. Phys. Lett.* **101**, 101910 (2012).
27. Monjezi, B. H. et al. Fast dynamic synthesis of MIL-68(In) thin films in high optical quality for optical cavity sensing. *ACS Nano* **17**, 6121–6130 (2023).
28. Ryder, M. R., Civalleri, B., Cinque, G. & Tan, J.-C. Discovering connections between terahertz vibrations and elasticity underpinning the collective dynamics of the HKUST-1 metal–organic framework. *CrystEngComm* **18**, 4303–4312 (2016).
29. Tricarico, M. & Tan, J.-C. Nanostructure-dependent indentation fracture toughness of metal-organic framework monoliths. *Next Materials* **1**, 100009 (2023).
30. Widmer, R. N., Bumstead, A. M., Jain, M., Bennett, T. D. & Michler, J. Plasticity of metal-organic framework glasses. *J. Am. Chem. Soc.* **143**, 20717–20724 (2021).
31. Zeng, Z., Xiao, Y., Wheeler, J. M. & Tan, J. C. In situ micropillar compression of an anisotropic metal-organic framework single crystal. *Commun. Chem.* **6**, 63 (2023).
32. Chaudhari, A. K., Han, I. & Tan, J. C. Multifunctional supramolecular hybrid materials constructed from hierarchical self-ordering of in situ generated metal-organic framework (MOF) nanoparticles. *Adv. Mater.* **27**, 4438–4446 (2015).
33. Hay, J. Instrumented indentation apparatus having indenter punch with flat end surface and instrumented indentation method using the same. *U.S. Patent* **10**, 288 (2019).
34. Tabor, D. Indentation hardness: fifty years on a personal view. *Philos. Mag. A* **74**, 1207–1212 (1996).
35. Tan, J. C., Merrill, C. A., Orton, J. B. & Cheetham, A. K. Anisotropic mechanical properties of polymorphic hybrid inorganic–organic framework materials with different dimensionalities. *Acta Mater.* **57**, 3481–3496 (2009).
36. Chen, S. et al. Intrinsic and extrinsic responses of ZIF-8 under high pressure: a combined raman and X-ray diffraction investigation. *J. Phys. Chem. C* **123**, 29693–29707 (2019).
37. Gigler, A. M. et al. Nanoscale residual stress-field mapping around nanoindenters in SiC by IR s-SNOM and confocal Raman microscopy. *Opt. Express* **17**, 22351–22357 (2009).
38. Ortiz, A. U., Boutin, A., Fuchs, A. H. & Coudert, F. X. Investigating the pressure-induced amorphization of zeolitic imidazolate framework ZIF-8: mechanical instability due to shear mode softening. *J. Phys. Chem. Lett.* **4**, 1861–1865 (2013).
39. Hu, Y. et al. Probing the structural stability of and enhanced CO₂ Storage in MOF MIL-68 (In) under high pressures by FTIR spectroscopy. *Chem. Eur. J.* **21**, 18739–18748 (2015).
40. Venkata Chalapathi, V. & Venkata Ramiah, K. Normal vibrations of N, N-dimethylformamide and N, N-dimethylacetamide. *Proc. Indian Acad. Sci. A* **68**, 109–122 (1966).
41. Jao, T. C., Scott, I. & Steele, D. The vibrational-spectra of amides—dimethyl formamide. *J. Mol. Spectrosc.* **92**, 1–17 (1982).
42. Qi, C., Wang, M., Bai, J., Wei, X. & Wang, H. Investigation into size and strain rate effects on the strength of rock-like materials. *Int. J. Rock Mech. Min. Sci.* **86**, 132–140 (2016).
43. Shahrin, R. & Bobko, C. P. Characterizing strength and failure of calcium silicate hydrate aggregates in cement paste under micropillar compression. *J. Nanomech. Micromech.* **7**, 06017002 (2017).
44. Yilmaz, E. D., Jelitto, H. & Schneider, G. A. Uniaxial compressive behavior of micro-pillars of dental enamel characterized in multiple directions. *Acta Biomater.* **16**, 187–195 (2015).
45. An, B., Wang, R., Arola, D. & Zhang, D. Damage mechanisms in uniaxial compression of single enamel rods. *J. Mech. Behav. Biomed. Mater.* **42**, 1–9 (2015).
46. Espinosa, H. D. et al. In situ wear study reveals role of microstructure on self-sharpening mechanism in sea urchin teeth. *Matter* **1**, 1246–1261 (2019).
47. Håkonsen, V., Singh, G., He, J. & Zhang, Z. Focused ion beam milling of self-assembled magnetic superstructures: an approach to fabricate nanoporous materials with tunable porosity. *Mater. Horiz.* **5**, 1211–1218 (2018).

Acknowledgements

A.M.K and C.B. thank The Engineering and Physical Sciences Research Council (EPSRC) grants entitled “Tackling human dental caries by multi-modal correlative microscopy and multi-physics modelling” (EP/P005381/1) and “Rich Nonlinear Tomography for advanced materials” (EP/V007785/1) for funding the research. J.C.T. and M.T. thank the ERC Consolidator Grant (PROMOFS grant agreement 771575) and EPSRC award (EP/R511742/1) for funding the research. We acknowledge the Diamond Light Source for the award of beamtimes SM34009 and SM32463 at MIRIAM beamline B22.

Author contributions

M.T. and J.C.T. conceived the project. M.T. synthesized and characterized the materials, performed nanoindentation test, processed the data and wrote the first draft of the manuscript under the supervision of J.C.T. MicroRaman measurements were performed by M.T., under the supervision of G.C. and J.C.T.; C.B. performed the FIB of micropillars under the supervision of A.M.K. All authors discussed the results and contributed to the final version of the manuscript.

Competing interests

The authors declare no competing interests.

Additional information

Supplementary information The online version contains supplementary material available at <https://doi.org/10.1038/s43246-023-00412-0>.

Correspondence and requests for materials should be addressed to Jin-Chong Tan.

Peer review information *Communications Materials* thanks the anonymous reviewers for their contribution to the peer review of this work. Primary Handling Editor: Jet-Sing Lee.

Reprints and permission information is available at <http://www.nature.com/reprints>

Publisher's note Springer Nature remains neutral with regard to jurisdictional claims in published maps and institutional affiliations.



Open Access This article is licensed under a Creative Commons Attribution 4.0 International License, which permits use, sharing, adaptation, distribution and reproduction in any medium or format, as long as you give appropriate credit to the original author(s) and the source, provide a link to the Creative Commons licence, and indicate if changes were made. The images or other third party material in this article are included in the article's Creative Commons licence, unless indicated otherwise in a credit line to the material. If material is not included in the article's Creative Commons licence and your intended use is not permitted by statutory regulation or exceeds the permitted use, you will need to obtain permission directly from the copyright holder. To view a copy of this licence, visit <http://creativecommons.org/licenses/by/4.0/>.

© The Author(s) 2023